Radio Science

RESEARCH ARTICLE
10.1029/2020RS007121

Bistatic Observations With SuperDARN HF Radars: First Results

S. G. Shepherd[1], K. T. Sterne[2], E. G. Thomas[1], J. M. Ruohoniemi[2], J. B. H. Baker[2], R. T. Parris[3], T. R. Pedersen[3], and J. M. Holmes[3]

[1]Thayer School of Engineering, Dartmouth College, Hanover, NH, USA, [2]Bradley Department of Electrical and Computer Engineering, Virginia Polytechnic Institute and State University, Blacksburg, VA, USA, [3]Space Vehicles Directorate, Air Force Research Laboratory, Kirtland AFB, NM, USA

Key Points:
- Bistatic capability has been developed and demonstrated using two midlatitude SuperDARN radars
- Three distinct propagation modes were commonly observed during bistatic campaigns
- Good agreement between observations and ray tracing using the IRI model is obtained

Correspondence to:
S. G. Shepherd,
simon.g.shepherd@dartmouth.edu

Citation:
Shepherd, S. G., Sterne, K. T., Thomas, E. G., Ruohoniemi, J. M., Baker, J. B. H., Parris, R. T., et al. (2020). Bistatic observations with SuperDARN HF radars: First results. *Radio Science*, 55, e2020RS007121. https://doi.org/10.1029/2020RS007121

Received 9 APR 2020
Accepted 18 JUN 2020
Accepted article online 27 JUN 2020

Abstract Super Dual Auroral Radar Network (SuperDARN) radars operate in a coordinated but monostatic configuration whereby high-frequency (HF) signals scattered from ionospheric density irregularities or from the surface of the Earth return to the transmitting radar where Doppler parameters are then acquired. A bistatic arrangement has been developed for SuperDARN radars in which HF signals transmitted from one radar are received and analyzed by another radar that is separated by a large distance (>1,000 km). This new capability was developed and tested on radars located in Oregon and Kansas. Numerous 3-day bistatic campaigns have been conducted over a period extending from September 2019 through March 2020. During these campaigns three distinct bistatic propagation modes have been identified including a direct mode in which signals are transmitted and received through the radar side lobes. Direct mode signals propagate along the great-circle arc connecting the two bistatic radar sites, reflecting from the ionosphere at both *E* region and *F* region altitudes. Two additional modes are observed in which HF signals transmitted from one radar scatter from either ionospheric density irregularities or from the surface of the Earth before propagating to the bistatic receiving radar. Ray tracing simulations performed for examples of each mode show good agreement with observations and confirm our understanding of these three bistatic propagation modes. Bistatic campaigns continue to be scheduled in order to improve technical aspects of this new capability, to further explore the physical processes involved in the propagation and scattering of HF bistatic signals and to expand the coverage of ionospheric effects that is possible with SuperDARN.

1. Introduction

The Super Dual Auroral Radar Network (SuperDARN) is an international collaboration that operates low-power, high-frequency (HF) scientific radars located in the midlatitude to polar regions of both hemispheres. The origins of the network can be traced to the construction of a single radar located in Goose Bay, Labrador (Greenwald et al., 1985). The network has expanded over the years to now consist of more than 35 radars of a similar design that are operated in a coordinated manner by scientists and funding agencies from ten different countries. SuperDARN radars are used individually and as a network in a variety of scientific experiments ranging from investigations of basic plasma phenomena to system-level science involving the large-scale plasma environment of Earth's ionosphere. Chisham et al. (2007) gives a detailed description of the variety of science topics addressed with SuperDARN. Nishitani et al. (2019) summarizes the recent accomplishments of the SuperDARN radars operating specifically in the midlatitude region.

SuperDARN radars are phased-array systems operating at HF to measure coherent backscatter from ionospheric density structures (e.g., Ruohoniemi & Greenwald, 1997). The standard operational mode involves the transmission of a multipulse sequence at a frequency between ~8–18 MHz in one of 16–24 azimuthal beam directions centered on the radar boresight and controlled by the radar phasing electronics. SuperDARN radars typically consist of a 16-element main antenna array with a beamwidth that is limited in the azimuthal dimension but broad in the vertical dimension (Sterne et al., 2011). Information about the elevation angle of returns is obtained with the help of a smaller four-element, receive-only interferometer array (Shepherd, 2017). Line-of-sight (LOS) Doppler velocity estimates are extracted from signals that are backscattered from ranges that can exceed 4,000 km. Backscatter from *F* region altitudes provide estimates of the convection electric field over local, regional, and large-scale areas (c.f. Ruohoniemi & Baker,

1998). The extended fields of view (FOVs) of SuperDARN radars are the basis for large-scale mapping of the ionospheric convection electric field (e.g., Ruohoniemi et al., 2001).

During the early stages of SuperDARN development, radars were built at sites close to ±60° AACGM latitude (Shepherd, 2014) with FOVs directed poleward to cover the high-latitude ionosphere. The radars were configured in pairs, separated by >1,000 km, with overlapping FOVs (Baker et al., 1989; Greenwald et al., 1995) in order to resolve the vector velocity within the common volumes. In more recent years the network has expanded so as to make observations in the polar (>70°) and midlatitude (>50°) regions (c.f. Nishitani et al., 2019), albeit in a somewhat more haphazard manner due, in part, to geological and logistical constraints. Nevertheless, radars now exist with many overlapping FOVs resulting in extensive coverage of the northern hemisphere above ~50° AACGM latitude, and somewhat less so in the southern hemisphere where suitable land is less abundant.

While there is significant coordination within the SuperDARN organization in the construction of radars and in operations and data sharing, the individual radars operate in a largely independent manner. Radars in the network collect data in common formats and follow a schedule of operation set by an internal SuperDARN committee, but each radar transmits and receives its own signal; that is, it operates in a monostatic fashion. In principle, it is possible for SuperDARN radars to also receive signals from other radars in the network, that is, to operate in a bistatic or even multistatic manner. In doing so the radars would gain many more paths for making observations, for observing plasma irregularities with different wave numbers, and for providing additional information about the characteristics of the irregularities and their associated Doppler velocities, with the potential for greatly expanding the area for resolving directly the two-dimensional velocity vector. We acknowledge that in practice it may require significant effort to realize bistatic operation between certain SuperDARN radars, which are composed of differing hardware and software.

Although there is considerable reference to bistatic measurements in the SuperDARN literature (e.g., Baker et al., 2007; Chisham et al., 2007; Wright & Yeoman, 1999; Yeoman et al., 2008), these studies actually refer to common-volume measurements from independent radars with overlapping FOVs that are operating monostatically. There is, however, one example of true bistatic observations that were carried out with the aid of a SuperDARN-style HF coherent scatter radar located in Ekaterinburg, Russia (Berngardt et al., 2015). In this study the SuperDARN-style radar transmitted signals that were received and analyzed by a radio telescope located more than 1,600 km away in Ukraine. One other related project that bears mentioning is the coordinated experiment between the Radio Receiver Instrument (RRI) on the Enhanced Polar Outflow Probe (e-POP) and the SuperDARN radar located in Saskatoon, Canada (SAS). In a preliminary study Perry et al. (2017) analyze individual pulses transmitted from SAS and received by RRI, located at an altitude of 380 km on-board the CAScade, Smallsat, and IOnospheric Polar Explorer spacecraft. While this study satisfies the definition of an example of bistatic radar operation, we restrict our attention to bistatic operation between two radars, specifically, SuperDARN radars.

The purpose of this paper is to report the details and results of a coordinated and successful effort to develop bistatic capabilities between two SuperDARN radars separated by a significant (1,819 km) distance. The paper is organized as follows: Section 2 describes various technical details of a bistatic operational mode for SuperDARN radars as well as experimental descriptions for numerous bistatic campaigns. Section 3 presents the first bistatic measurements from two SuperDARN radars highlighting the three distinct modes of propagation that have been observed. We compare results from ray tracing simulations to the observations and find good agreement that confirms our understanding and interpretation of the bistatic observations. Section 4 summarizes our work and describes future plans and challenges for expanding bistatic operations to the rest of the network.

2. Bistatic Description

Two radar sites located near Christmas Valley, Oregon and Fort Hays, Kansas were chosen for the project. Constructed under the National Science Foundation (NSF) Mid-Sized Infrastructure (MSI) program in the early part of the decade, these were the first two sites to host pairs of colocated SuperDARN radars (identified by three-letter radar codes: CVW/CVE and FHW/FHE), which share common hardware. The radars, CVE and FHW, were chosen for the project because of their large overlapping FOVs and their nearly identical

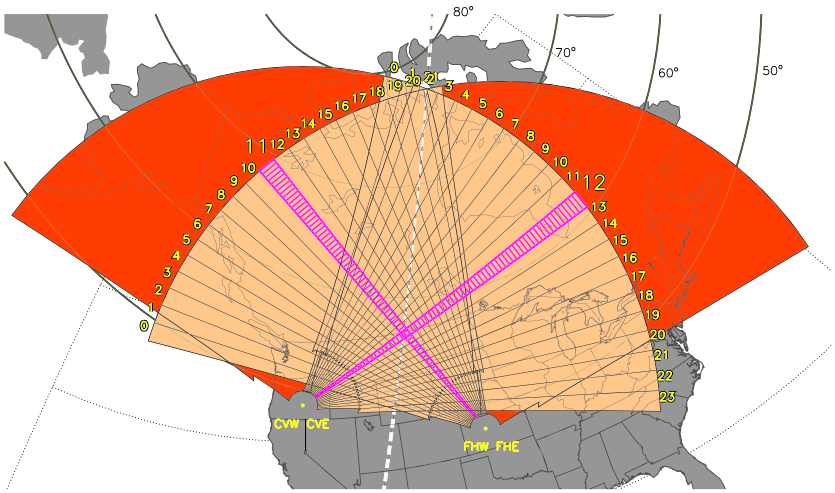

Figure 1. FOVs from SuperDARN radars located at Christmas Valley, Oregon and Fort Hays, Kansas where bistatic operations were developed. Bistatic radars (CVE and FHW) are shown in light orange with nominal beam directions (numbered in yellow), emphasizing a large overlapping region. A sample beam pairing is highlighted in magenta with standard 45-km range resolution shown. Nonbistatic radar FOVs (CVW and FHE) are shown in darker orange. A dashed white line marks the site bisector; points that are equidistant from each site.

electronics and software. Figure 1 shows the radar FOVs and the large overlapping region for supporting common volume and bistatic operations.

One important detail about the bistatic operation described here is that one of the bistatic radars was operated in a receive-only manner. While it is possible to transmit and receive on both bistatic radars simultaneously, it would be difficult in that case to determine which radar was the source of any observation. In order to eliminate this ambiguity we chose to operate CVE in a receive-only manner while otherwise functioning normally but transmitting no power. The other bistatic radar (FHW in this case) operated normally; that is, it both transmitted and received its own signal.

The choice of CVE as the receive-only radar was made, in part, because this site has an operational interferometer array; a smaller four-element antenna array that is offset from the main 16-element array and is used to infer the elevation angle of the received signals (Shepherd, 2017). For bistatic operations it was deemed more desirable to have elevation angle measurements at the receive end of the link to help resolve the propagation mode.

An important technical detail necessary for making bistatic measurements with SuperDARN radars is the synchronization of timing between the radars. To obtain range information from a distributed scattering region the SuperDARN radars utilize a multipulse transmission sequence that is analyzed to provide Doppler information (power, LOS velocity, and spectral width) over ranges often exceeding 4,000 km (e.g., Ribeiro et al., 2013). Signal-to-noise ratio (SNR) is improved by integrating multiple transmission sequences in a given beam direction. Typical integration periods are 3–7 s yielding 20–70 sequences. These sequences must be synchronized at both radars in order to make sense of the bistatic measurements.

For SuperDARN radars the range resolution along a beam direction is nominally determined by the length of individual pulses in the sequence and is typically 100–300 μs, corresponding to 15- to 45-km range resolution, respectively. Range resolutions as small as ~6 km have been achieved with pulse-coding schemes; however, the pulse width remains in the 100- to 300-μs range. Bistatic measurements require that the timing difference between the sites be limited to a small fraction of the pulse width, that is, <10 μs.

Network Time Protocol (NTP) is capable of maintaining time to within tens of milliseconds, which is not sufficiently accurate for our purposes. Instead, we use timing clocks in the radar computers that are synchronized using Global Positioning System (GPS) signals. Specifically, a GPS card installed in the computer that interfaces to the radar electronics at each site is used to generate regular timing pulses. The timing pulse initiates a sequence of timing signals that direct the various hardware components to generate and transmit

HF pulses and to receive and digitize incoming signals. We have found that GPS pulses generated at 7 Hz work well for bistatic operations.

Preliminary testing has confirmed that the timing pulses from this GPS synchronization occur within ±5 μs of each other at the respective radar sites. The result is a better than 95% overlap of the transmission windows, even though one site is in receive-only mode. This level of synchronization is sufficiently accurate to support bistatic operations.

Before bistatic operation was first attempted, additional testing was performed at each radar site in order to eliminate the possibility of any coupling occurring between the collocated antenna arrays. For these tests the radar at each site that was not to be involved in the bistatic experiment (e.g., CVW and FHE) was set to operate monostatically (transmitting and receiving its own signal) while the second radar at the same site (e.g., CVE and FHW) was put into a bistatic mode where it simply received signals. It was confirmed that signals are indeed observed on the receive-only radars when the two collocated radars operate at identical frequencies. Coupling in this case maximizes when the main lobes of the collocated radars are pointed in the same direction, that is, along the bisector of the two array axes. Note that the MSI dual radars were designed with radar boresights separated by 70°–75° from each other symmetrically about the radar bisector, which is directed toward the north magnetic pole. Coupling occurs through radar side lobes and is greatly reduced when the radar main lobes are directed away from the common direction. For these reasons a frequency separation of ∼50 kHz is imposed during all operations at the dual-radar sites, including during bistatic operations. When frequency separation is enforced, it is confirmed that no significant coupling occurs between the radars.

Initial testing was conducted with the nonbistatic radars (CVW and FHE) remaining idle. However, during subsequent preliminary testing and bistatic campaigns these radars were operated in the standard manner (monostatic) in order to collect information about ionospheric propagation conditions and plasma flow over a larger region to provide contextual information for the bistatic observations.

After a limited amount of exploratory bistatic operation in which the operating frequency and beam combinations of the bistatic radars (CVE and FHW) were changed in a relatively ad hoc manner, a series of 3-day bistatic campaigns were implemented at the two sites. These campaigns were run during so-called discretionary time (DT) in the SuperDARN operating schedule. DT intervals, total 9 days each month, are scheduled around other experimental requests and typically occur on consecutive 3-day periods. During DT periods SuperDARN PIs are free to perform maintenance on their radars, test experimental radar modes or operate their radars in any nonstandard manner they choose.

Beginning in September of 2019 the PI groups of the Oregon (CVW/CVE) and Kansas (FHW/FHE) sites scheduled their radars to operate in a bistatic manner during DT periods. For these campaigns a variety of experiments were performed in which the bistatic radars (CVE and FHW) operated on a preselected, common frequency (that could be varied in time) over a limited number of beam directions (ranging from 10 to 20). The nonbistatic radars (CVW and FHE) operated in the standard manner with the number of beam directions (or beams) during a radar scan (sampling of beams in a 1- to 2-min period) chosen to be commensurate with their bistatic pair. All the radars at these sites operated with GPS time synchronization during the periods of bistatic operation.

Several different bistatic campaign scenarios were performed including operating at a single fixed frequency for a 24-hr period, transitioning between night (10.8 MHz) and day (13.8 MHz) frequencies and a frequency stepping arrangement whereby the bistatic radars operated for a 1-hr period at one of four set frequencies: 10.725, 11.8, 13.8 and 15.8 MHz. In most cases, the bistatic radars sampled 20 beams in a single 1-min scan corresponding to ∼3 s integration per beam. The beams were chosen to be directed into the common-volume area of the two radars with a clockwise scanning sense for CVE (beams: 4–23) and counterclockwise for FHW (beams: 19–0).

Figure 1 shows two representative beams during the middle of a typical scan, with the two beams intersecting very near the radar site bisector line (dashed white trace). This symmetric beam pairing is the simplest to analyze since the paths between the radars and a common scattering point are then roughly the same. With the timing of the two radars synchronized for transmit and receive, CVE receives signals transmitted by FHW at the ranges that would be expected if it transmitted its own signal, assuming similar propagation

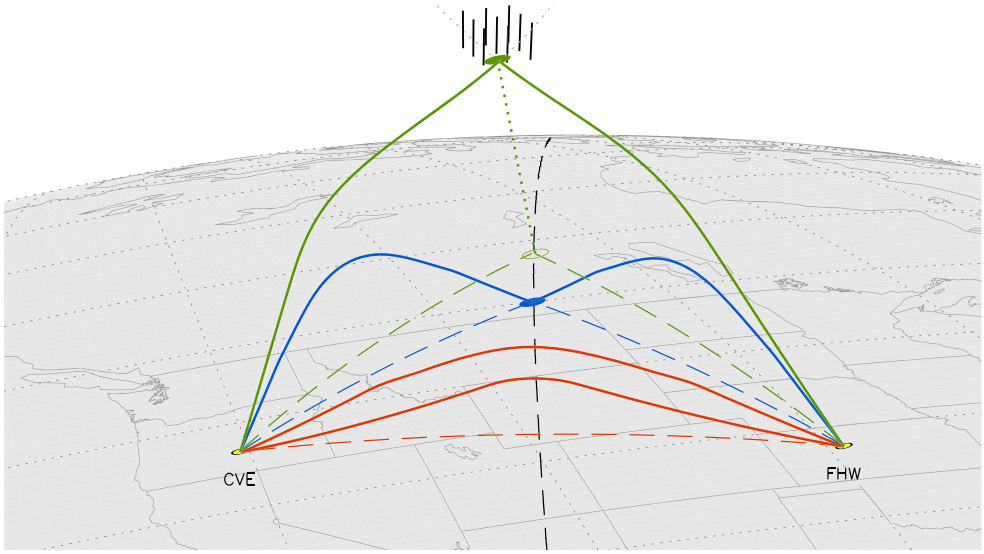

Figure 2. Schematic of three bistatic propagation modes: direct (red), bistatic GS (blue) and bistatic IS (green). Solid lines indicate raypaths, with dashed colored lines the corresponding path projection onto the Earth; solid colored circles are scattering locations (black line segments above surface represent ionospheric irregularities). The black dashed line is the site bisector.

and scattering conditions along the two paths. This mode has been used during most of the bistatic campaigns. The results shown in section 3 were observed using this symmetric beam configuration, however, some campaigns have been conducted with nonsymmetric configurations. While the analysis is more difficult due to the differing propagation path lengths in this scenario, results from these campaigns are expected to reveal a more complete picture of the propagation and scattering conditions required to satisfy bistatic operations at HF. Analysis of bistatic observations with nonsymmetric beam configurations is left for a future study.

3. Bistatic Results

Bistatic operations have now been performed for a total of ~45 days beginning in September of 2019 and continuing in 2020. Observations have occurred under a range of geomagnetic conditions and a variety of bistatic modes have been identified. While the observations are sufficient for statistical analyses, we leave that task for subsequent studies. Here, we present examples and details of the three distinct modes of propagation that were frequently observed during the bistatic campaigns. Briefly, these modes are (1) direct transmission between the radar sites (direct mode), (2) bistatic ground scatter (bistatic GS) and (3) bistatic ionospheric scatter (bistatic IS).

Figure 2 shows a schematic that illustrates the basic concept of these three bistatic modes. The direct mode is shown in red, bistatic GS in blue and bistatic IS in green. Solid lines of these colors represent raypaths that signals travel in the respective modes. Note that while bistatic signals travel from FHW to CVE for the majority of the bistatic campaigns, the reverse is also possible. Dashed, colored lines are projections of the raypaths onto the Earth. The site bisector is marked by a black, dashed line. For the direct mode there are two paths that follow the great-circle arc between the sites as shown in Figure 2. These paths correspond to refraction back toward the ground occurring at *E* region and *F* region altitudes, respectively. There is no scattering involved in this mode and despite separate paths we do not consider them separate modes because the basic mechanism is the same.

For the other two modes (bistatic GS and bistatic IS), refraction occurs but scattering is also required. For the bistatic GS mode signals are refracted back to the ground and scattering occurs from surface roughness (André et al., 1998). The scattering location for this mode is shown in Figure 2 by a solid blue circle. At this location some of the wave power is backscattered to the transmitting radar and some is scattered to the

10.1029/2020RS007121

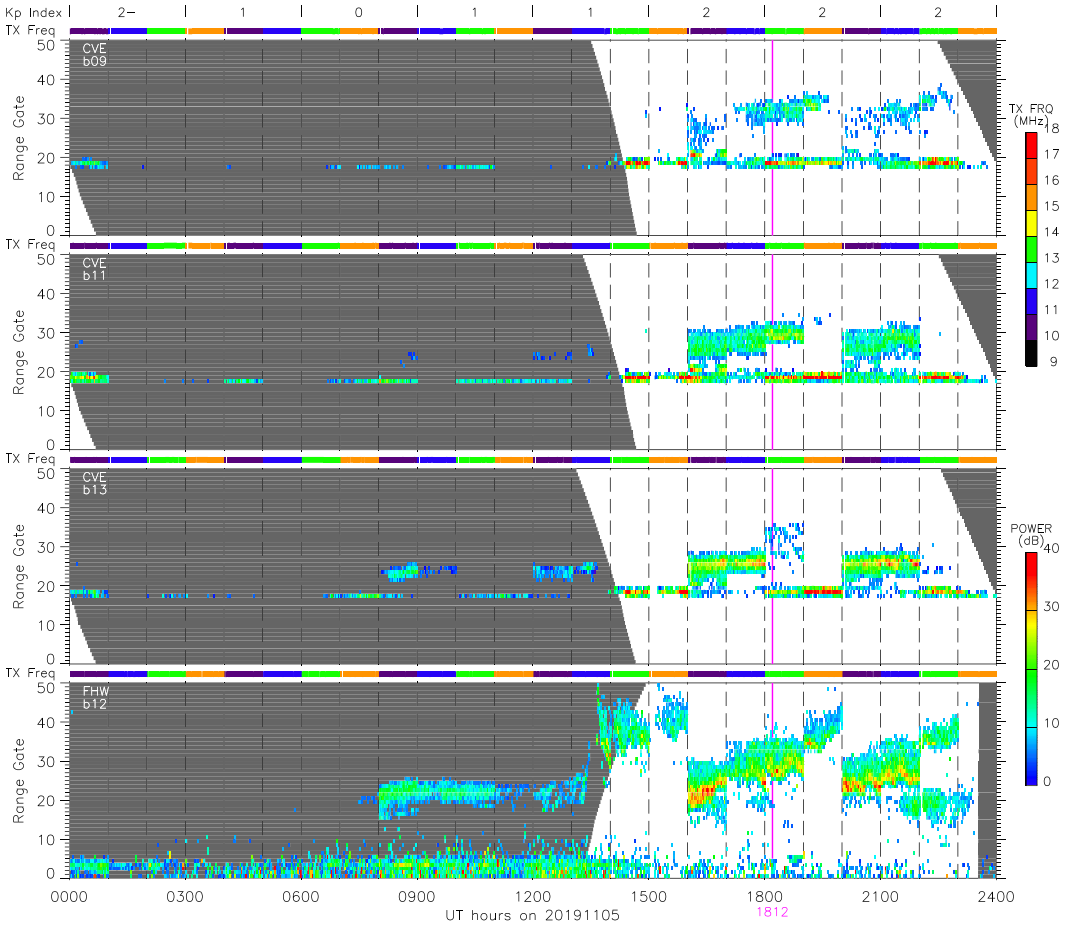

Figure 3. The 24-hr period of bistatic observations from beams 9, 11, and 13 of CVE and monostatic backscatter from beam 12 of FHW SuperDARN radars on 5 November 2019. Vertical scale indicates 45-km range gate number. Color scale indicates signal level in dB above sky noise, shown in lower color bar. Operation frequency indicated by color strip above top panel and in upper color bar. The 3-hr Kp index values are shown above the top panel. Gray background indicates darkness. Visible in the top three panels are three propagation modes: direct mode in range gates 18–20, bistatic GS at further ranges during daytime hours and bistatic IS during nightime hours. Data from FHW in the bottom panel shows monostatic backscatter from the ground, ionosphere and meteors during this period. A magenta line at 18:12 UT highlights an interval for further study.

bistatic receiver. The mechanism for the bistatic IS mode is similar, however, the scattering occurs from ionospheric plasma density irregularities (Fejer & Kelley, 1980), represented by black line-segments above the solid green circle in Figure 2, marking the scattering location for this mode.

Many examples of these modes, often occurring simultaneously, were observed during the bistatic campaigns. Having selected representative examples of each mode, we show the observations and perform ray tracing simulations in order to confirm our understanding of the basic mechanisms for these bistatic modes of propagation.

Figure 3 shows observations from CVE and FHW over a 24-hr period during a campaign on 5 November 2019. The data shown are for beams 9, 11, and 13 of CVE and beam 12 of FHW (see beam numbers in Figure 1), from top to bottom. The color indicates the strength of the signal in dB above the sky noise. The vertical axis indicates the 45-km range gate number of the measurements with the upper limit corresponding to just below 2,500 km in range from the radar site.

To be clear, all the signals observed by CVE originated from FHW and thus constitute bistatic signals. During this particular period the bistatic radars were stepping through a set of four frequencies (10.725, 11.8, 13.8 and 15.8 MHz) with the frequency remaining fixed for an hour at a time. Significant variability was

observed in the strength of the bistatic signal as the frequency was changed. Additional variability was seen within the 1-hr intervals of fixed frequency operation that was due to geophysical processes affecting the propagation path of the signal and possibly also to timing registration issues at the two sites. Observations from the three CVE beams shown in the top panels of Figure 3 reveal additional variability that is due to differing beam geometries and propagation conditions.

For the period shown in Figure 3 all three of the bistatic modes are observed. The direct mode can be seen during much of the 24-hr period and in all three panels of CVE data. It occurs in the narrow band of range gates from 18–20 corresponding to a range interval from ~990–1,080 km. The bistatic GS and IS modes are more intermittent and seen at farther ranges and over a wider range interval, ~1,080–1,980 km. In this example, the bistatic GS mode is observed primarily during daytime hours and has a wider range extent than the bistatic IS mode that is seen during nighttime hours over a somewhat narrower range extent. All three modes show significant variability with frequency, beam direction, and time of day.

The bottom panel in Figure 3 shows monostatic backscatter along beam 12 of FHW occurs from meteors in the nearest ranges for the entire period, from ionospheric irregularities during nighttime hours, and from the ground during daytime hours. The observed overlap in monostatic backscatter and bistatic scatter is discussed further in sections 3.2 and 3.3 where the bistatic GS and IS modes are investigated in more detail.

3.1. Direct Mode

The direct transmission mode is the name we give to signals that are transmitted from one radar (FHW) and propagate through the ionosphere directly to the receiving radar (CVE) following a great-circle arc. This mode is similar to that of an oblique sounder with one difference being that we are operating at a single frequency. This mode would presumably occur when the bistatic radars were operating with beams pointing directly at each. There is, however, no such beam combination (see Figure 1) and given that this mode is observed at a constant range over all of the beams in a 2-min scan, we surmise that the direct mode occurs through the radar side lobes.

Figure 4 shows a 2-min period of data from the Oregon (CVW/CVE) and Kansas (FHW/FHE) radars from 18:12–18:14 UT on 5 November 2019 (indicated by the vertical magenta line in Figure 3). The bistatic radars (CVE and FHW) were operating at 13.8 MHz during this period, while CVW was operating at 14.7–15.0 MHz and FHE was operating at 11.4–11.6 MHz. The observed Doppler LOS velocity (v_{LOS}) is shown according to the blue-red color scale. Low-velocity magnitude ($<10\ m\ s^{-1}$) is indicated with light gray for nonbistatic radars (CVW and FHE), darker gray for FHW and green for CVE. Furthermore, the bistatic observations from CVE are highlighted in yellow outline for clarity.

During this period the nonbistatic radars and FHW were observing bands of ground or sea backscatter that extended over the entire azimuthal extent of the radar FOVs. Ground scatter, as it is commonly referred to, occurs when signals transmitted by a radar refract sufficiently in the ionosphere so that they propagate back to the ground (or sea) at some distance from the radar. There, the signals encounter roughness and some power is scattered back to the radar. The so-called skip distance is the distance on the Earth's surface that the signals travel between the radar and the point where they are reflected from the ground. Because the skip distance depends on the radar frequency and the density of the ionosphere, ground scatter can be used to determine ionospheric conditions in the radar FOV (Hughes et al., 2002). In addition, ground scatter often reveals details of atmospheric gravity wave activity associated with traveling ionospheric disturbances as the observed skip distance is modulated by changes in the ionospheric density (Samson et al., 1990).

The direct mode, as seen in Figure 4, occurs over a constant range interval (three range gates in this example) over the entire scan of CVE radar beams. Here we are using the standard SuperDARN analysis software, commonly referred to as the Radar Software Toolkit (RST) (Thomas et al., 2019), which is designed for monostatic operation and, therefore, maps the position of signals based on the assumption of round-trip propagation. For this reason the direct mode observations appear at a distance that is half of the actual travel distance, that is, at the halfway point along the great-circle arc between the bistatic radars.

The direct mode appears at a constant range because the propagation path between the radars is relatively constant through the side lobes while the software assumes the observations are in the direction of the main lobe. The result is the arc, colored green for low velocity, appearing in range gates 18–20. Variations in the signal strength with time and beam direction (seen in Figure 3) can be attributed to operational factors, such

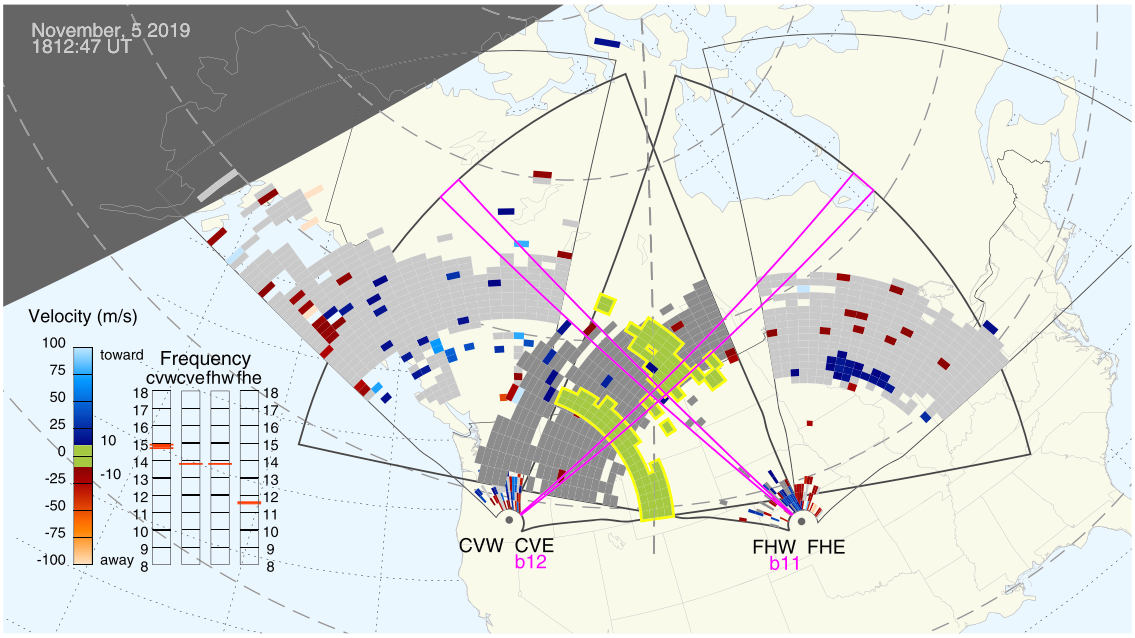

Figure 4. SuperDARN observations for a 2-min period from 18:12–18:14 UT on 5 November 2019 during a bistatic campaign. LOS Doppler velocity is shown according to the red-blue color scale, with low velocity (<10 m s^{-1}) indicated by gray and green colors. Light gray is used for nonbistatic radars (CVW and FHE), darker gray is used for the transmitting bistatic radar (FHW) and green is used for the receiving bistatic radar (CVE). All bistatic observations (CVE) are highlighted with a yellow outline for clarity. Two distinct bands of bistatic measurements are observed, corresponding to different propagation modes: direct mode in the near ranges and bistatic GS in the farther ranges. Bistatic radars (CVE and FHW) were operating at 13.8 MHz.

as the relative side lobe strength of a particular beam combination, and the operating frequency. Note that side lobes can be as high as -10 dB in certain situations (Sterne et al., 2011). In addition, some of the variation is clearly geophysical in nature as the ionospheric density changes along the propagation path due to external influences, the most obvious being the very strong signals observed during the daytime at the higher frequencies when the ionospheric densities are largest.

In order to understand the details of signals propagating between the radars in the direct mode, we performed ray tracing simulations of the HF signal in a model ionosphere given by the latest version of the International Reference Ionosphere (IRI-2016) (Bilitza et al., 2017). The ray tracing code is a modified version from de Larquier et al. (2013), which uses an adaptive step size Runga-Kutta solver to determine the raypaths of HF waves in an unmagnetized plasma.

Figure 5 shows the results of the ray tracing simulations for the conditions given by the IRI-2016 model and the operational radar parameters used at 18:12–18:14 UT on 5 November 2019. The background color indicates the electron density given by the IRI-2016 model along the great-circle path between the two bistatic radars. Two representative electron density profiles, on a logarithmic scale, are shown at 0- and 1,819-km ground range. Projections of the magnetic field from the International Geomagnetic Reference Field (IGRF) (Thébault et al., 2015) are indicated with pink lines spaced at 500-km intervals at 400-km altitude.

In this simulation a set of rays consisting of electromagnetic waves at 13.8 MHz are launched from the location of CVE with elevation angles ranging from 0° to 35°. The decision to have the rays originate from CVE was chosen for simplicity in determining elevation angles. Reciprocity is assumed and the elevation angles on receive are therefore the same as the launch angles, which are specified for each ray.

The paths of representative rays are shown in gray, with darker gray used to indicate penetrating rays, that is, rays that do not return to the surface of the Earth. Rays that return to the ground within ±45 km (one range gate) of the location of FHW are highlighted in magenta. These rays represent potential paths for signals to travel directly between the two radars. Note that the vertical scale in Figure 5 is doubled in order to emphasize the region of interest in the ionosphere while showing the entire raypath; as a consequence, some raypaths may appear distorted.

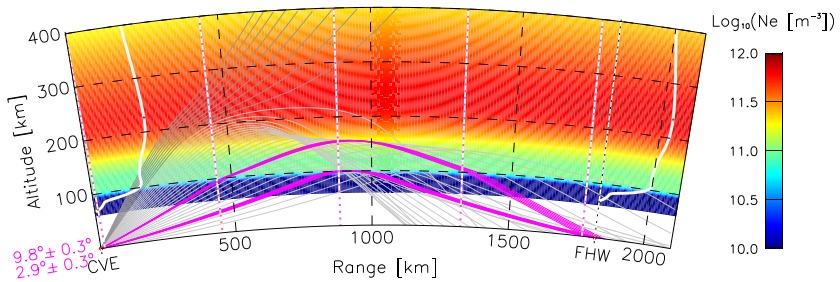

Figure 5. Ray tracing simulation of the direct mode at 18:12 UT on 5 November 2019. The background color indicates the electron density specified by the IRI-2016 model in a two-dimensional plane along the great-circle between bistatic radars CVE and FHW. Representative raypaths are shown in gray. Rays showing two potential direct mode propagation paths that reflect in the *E* and *F* regions are highlighted in magenta. These rays return to the ground within ±45 km of the location of FHW. The mean and range of elevation angles from these rays are given near their origin.

It is evident from these simulations that two possible paths exist for the direct mode: one that refracts back toward the ground in the *E* region and another that does the same at a higher altitude in the *F* region. Rays traveling along the longer *F* region path would appear at ranges further from the radar than those traveling along the shorter *E* region path. If both paths exist at a given time, one might therefore expect observations of the direct mode at multiple ranges. We suggest that this situation explains the direct mode being observed over three range gates during the daytime in Figure 3. An example of two simultaneous, yet separated in range, observations of the direct mode was captured when a bistatic campaign was operated with 15-km range resolution. This aspect of bistatic propagation is the focus of an ongoing study, and we include only a brief example from this period here.

Figure 6 shows a 3-hr period (15:00–18:00 UT) of CVE bistatic observations of the direct mode along beam 20 for two consecutive days: 25 and 26 February 2020. In the top panel, the bistatic radars were operating with 15-km range resolution using 100-μs pulses, while in the bottom panel they were operating with the standard

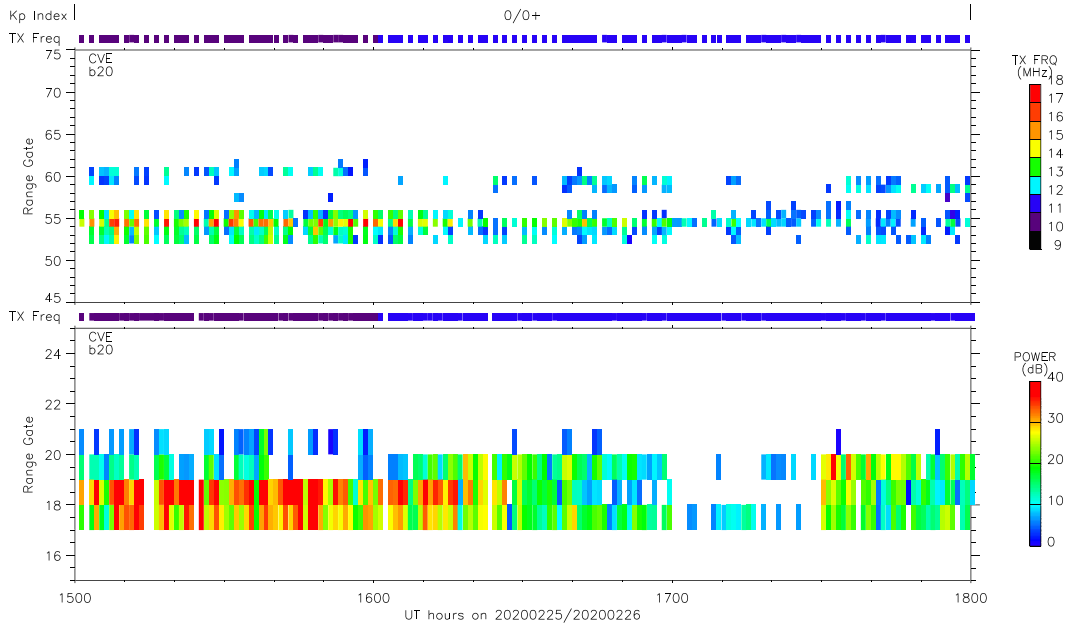

Figure 6. A 3-hr period of bistatic observations from beam 20 of CVE SuperDARN radar on 25 (top panel) and 26 (bottom panel) February 2020. Vertical scales indicate 15 and 45-km range gate number, respectively. Format is the same as in Figure 3. Two distinct bands in the 15-km range resolution data, which appear as a single band in the 45-km range resolution data, suggest that both *E* region and *F* region propagation paths exist.

45-km range resolution using 300-μs pulses. Geomagnetic conditions were very quiet on both days as indicated by the Kp index values of 0 and 0+ on respective days.

Of particular note is the difference between the observations under similar conditions but with different range resolution. In the upper panel, using 15-km range resolution, there are two distinct bands that are separated by several range gates, whereas in the lower panel the observations cover the same range extent but appear primarily as a single band. While there is significant variability in the observed power in both cases that depends on both range and time, the two bands observed with 15-km range resolution suggest that propagation via both *E* region and *F* region paths are indeed occurring, as predicted by the ray tracing simulations.

Note that while the simulations suggest that *E* region and *F* region propagation paths can be resolved by measuring elevation angles of signals at the bistatic receiver (~3° for *E* region and ~10° for *F* region), further analysis is required to resolve elevation angles for direct mode propagation. These signals are communicated through radar side lobes and the elevation angles determined by the RST are assumed to be from the main lobe direction of the phased arrays.

3.2. Bistatic Ground Scatter Mode

The other bistatic mode observed at 18:12 UT in Figures 3 and 4 is the bistatic GS mode. This mode is similar to ground backscatter observed during monostatic operation; however, the signal observed by the bistatic receiver originates from the bistatic transmitter and is scattered from the location on the ground where the rays are reflected in the direction of the bistatic receiving radar. Figure 4 (and to some extent Figure 3) reveals that the bistatic GS mode is observed where the bistatic beams overlap in an area where ground backscatter is observed by the transmitting radar operating in monostatic mode, that is, FHW.

During the period shown in Figure 4, the bistatic radars were operating with symmetric beam pairings and the beams, therefore, intersect along the bisector of the two radar sites. The overlapping region in this case occurs where the radar bisector intersects the ground backscatter band observed by the transmitting radar. In this situation the paths to the scattering point are similar and bistatic observations are only possible where ground backscatter is also occurring along the transmission leg. The location of the bistatic GS observations will, therefore, move as the location of the ground backscatter (skip distance) responds to changes in the density of the ionosphere and the operating frequency.

It can be seen in Figure 4 that radars are operating at different frequencies and as a consequence both the skip distance of their respective ground backscatter bands, and the extent of the bands, differ. In this case the skip distance is proportional to the operating frequency, whereas the range extent varies inversely with frequency. Ground backscatter appears closest to the FHW radar that is operating at the lowest frequency (~11.5 MHz) during this time and the extent of the band is the greatest. Note that some deviation from this expected behavior is observed in the zonal directed beams of CVW and FHW. These beams sample parts of the ionosphere that are very different from those sampled by the poleward directed beams, which illustrate the expected dependence.

Figure 3 shows that bistatic GS observations (top three panels) track variations in the transmitting radar skip distance (bottom panel) as the frequency changes at hour intervals. In the daytime hours the band of bistatic GS observations narrows in extent and increases in range as the frequency increases, as expected.

We investigate the statistical properties of the V_{LOS} and spectral width parameters for several 1-hr intervals when the bistatic GS mode is observed. The weighted mean V_{LOS} is found to be $<1\ m\ s^{-1}$ with standard deviation $<5\ m\ s^{-1}$. The spectral width parameter, which represents decorrelation of the coherent signal, is found to be similarly small over the hourly periods. These values are consistent with those from the three radars operating monostatically during the same periods and confirm that the low velocity, low spectral width characteristics of the bistatic GS mode measurements are consistent with scattering from the ground (Blanchard et al., 2009; Chisham & Pinnock, 2002).

As with the direct mode, we perform a ray tracing simulation using the ionospheric density specified by the IRI-2016 model during the time when the bistatic GS mode was observed. Unlike the monostatic or direct mode situation rays in the bistatic GS mode propagate along two separate paths through the ionosphere. We leave a full three-dimensional ray tracing simulation to a future study and instead perform ray tracing

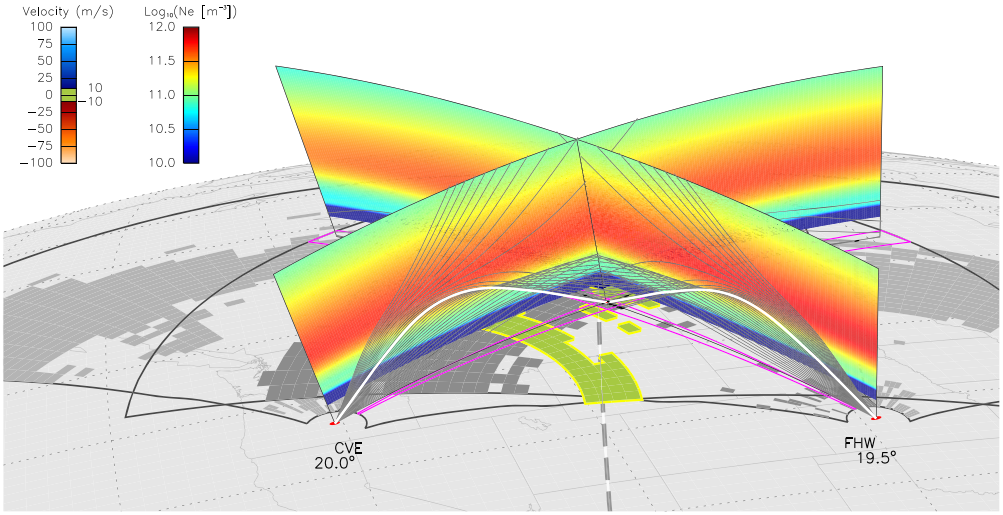

Figure 7. SuperDARN observations and ray tracing simulations at 18:12 UT on 5 November 2019. Bands of ground scatter observed on the monostatic radar are indicated by gray in the radar FOVs. Observations of the direct mode and bistatic ground scatter are indicated with green and highlighted with a yellow outline. Ray tracing simulations along representative beam directions from CVE and FHW indicate raypaths (highlighted in white), which coincide at the reflection point on the Earth and confirm a viable path for bistatic ground scatter observations.

along separate two-dimensional planes in the directions of the bistatic radar beams. In this case we propagate rays originating from both bistatic radar sites (CVE and FHW) and look for those rays that return to the ground within one 45-km range gate of the beam intersection location.

Figure 7 shows the results of the ray tracing simulation for the 1-min period starting at 18:12 UT on 5 November 2019. Measurements from the four radars are shown on the map. The ionospheric density obtained from the IRI-2016 model is shown along two representative beam directions (CVE: 12, FHW: 11). Rays with elevation angles in the range 0°–35° are shown in gray. Some of these rays penetrate the ionosphere and others return to the ground at a distance from the radars. The rays that return to the ground within the beam intersection region are highlighted in white. Collectively, these are the possible paths for bistatic signals to propagate from FHW to CVE in the bistatic GS mode. Simulations along the other beam combinations occurring during this period indicate that a viable path for the bistatic GS mode exists in the region where the beam intersection overlaps the ground backscatter band from the transmitting radar.

As was the case for the direct mode we made no modification to the densities obtained from the IRI-2016 model for these simulations. While a more careful analysis might entail modifications to the model predictions based on, say, density profiles obtained from ionosonde data, we emphasize that these results support the idea that the bistatic GS mode is the most likely explanation for the bistatic measurements obtained during these periods.

One other measurable we are able to compare with the output of the simulations is the elevation angle. Figure 7 shows that the elevation angles at CVE satisfying the criteria for the bistatic GS mode during this period were within a degree of 20°. This value was the maximum obtained from simulations of the other beam combinations, which also showed the elevation angle decreasing as the intersection point moves further from the radars.

Measurements of elevation angles require estimates of the relative phase difference between the signals arriving at the main and interferometer arrays, each of which are subject to statistical fluctuations. Individual measurements of the elevation angles are, therefore, somewhat less reliable than the corresponding Doppler parameters derived from signals on the larger main array. For this reason we look at elevation angles for the 1-hr period 18:00–19:00 UT in order to increase the statistics, particularly for the bistatic observations.

Figure 8 (left panel) shows histograms of the elevation angle occurrence during this period for beam 11 of both CVW and CVE in blue and orange, respectively. Observations are limited to range gates 25–50 and

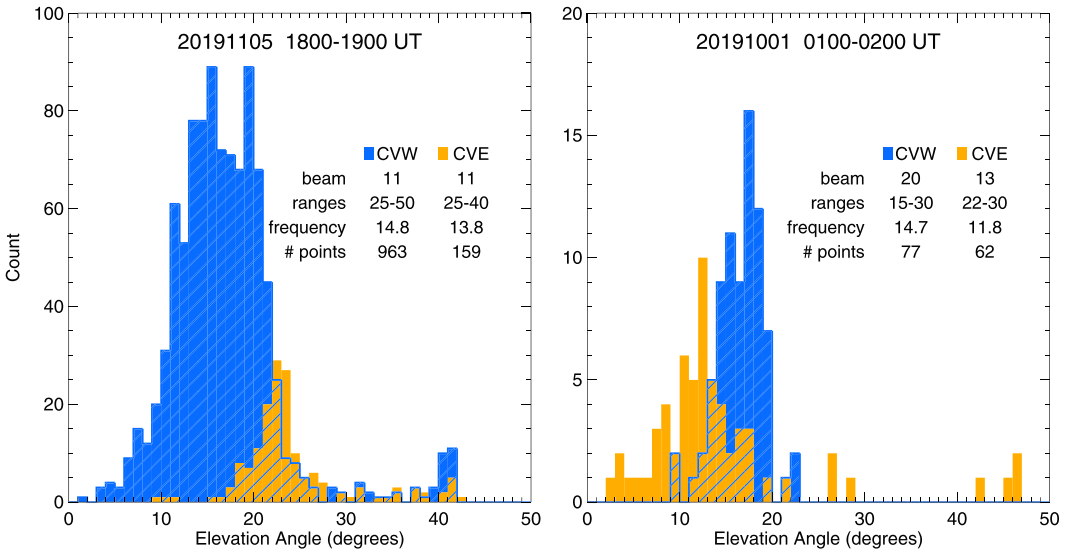

Figure 8. Histograms of elevation angle occurrence for CVW and CVE during the 1-hr periods 18:00–19:00 UT on 5 November 2019 (left panel) and 01:00–02:00 UT on 1 October 2019 (right panel) shown in blue and orange, respectively. Histograms are for a single beam and limited ranges; both given in the respective panels.

25–40, respectively, to ensure that only ground backscatter and bistatic GS mode measurements are included in the two samples. The number of samples for CVW is significantly larger than for CVE due, in part, to the somewhat broader extent in range of ground backscatter and also the fact that CVW was sampling each beam every one minute compared to every two minutes for CVE. The distribution of elevation angles observed by CVW show a broad peak (~10° wide) in the range of ~12°–22°. These measurements are consistent with expectations for ground backscatter (Ponomarenko et al., 2015). The distribution of elevation angle measurements from CVE shows a well-defined and narrower peak (~3° wide), likely due to the localization of these bistatic measurements along the radar bisector, at ~22.5°.

The agreement between the observed elevation angles and those obtained from the ray tracing simulation are generally good, supporting the idea that the observations are indeed propagating in the bistatic GS mode. There are, however, differences that are not unexpected since IRI is an empirical climatological model and likely differs from the actual ionosphere, even for the very quiet geomagnetic conditions during this period. Another source of the observed differences is the possibility that the radars require further calibration for the accurate measurement of elevation angles (cf. Shepherd, 2017, pp. 940–941).

3.3. Bistatic Ionospheric Scatter Mode

The third propagation mode observed during our campaigns we refer to as bistatic IS. In this case signals transmitted from FHW scatter from ionospheric irregularities at *F* region altitudes and return to the bistatic receiver at CVE, in addition to returning to the transmitting radar. In this scenario, as with the monostatic situation, the Doppler velocity of the received signals is a measure of a component of the $\vec{E} \times \vec{B}$ plasma drift.

While the bistatic IS mode was observed on 5 November 2019 (Figure 3) during nighttime hours, we choose an example from another period on 1 October 2019 to investigate this mode in more detail. Figure 9 shows observations for the 24-hr period on this day from a single beam of all four SuperDARN radars located in Oregon and Kansas. From top to bottom, the selected beams are CVW beam 18, CVE beam 13, FHW beam 10, and FHE beam 5. Overall geomagnetic activity is greater during this period as indicated by Kp values ranging from 2+ to 4 during the first 12 hours. Relatively strong and highly variable flows exceeding 100 m s^{-1} can be seen in the nonbistatic radars (CVW and FHE) for the early part of the period, up to ~08:00 UT. The sense of flow during this period is in the westward direction as indicated by the red/blue colors of west/easterly directed beams of the CVW/FHE radars shown in the top/bottom panels of Figure 9.

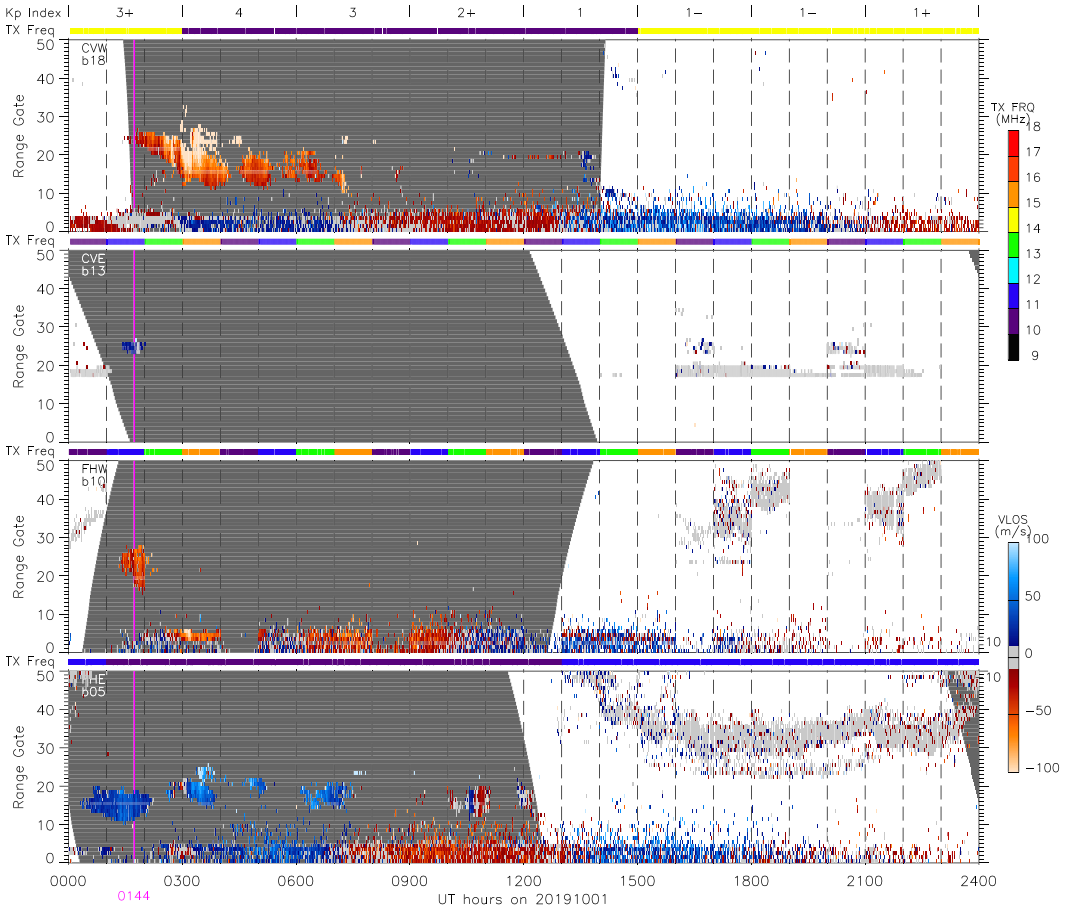

Figure 9. The 24-hr period of observations on 1 October 2019 from one beam of each SuperDARN radar in Oregon and Kansas: CVW beam 18, CVE beam 13, FHW beam 10, and FHE beam 5. The format is the same as in Figures 3 and 6; however, here we are displaying V_{LOS} according to the lower color scale, with blue and red representing motion toward and away from the radar. Supporting radars CVW and FHE show flows exceeding 100 m s^{-1} during the more active period from dusk to midnight. Bistatic radars CVE and FHW are stepping in frequency and observe a period of bistatic IS mode scatter between 01:00 and 02:00 UT. A period at 01:44 UT, marked by a magenta line, is selected for further study.

The interval of interest on this day begins near 01:30 UT and continues for approximately 30 min. During this time the bistatic radars were operating at 11.8 MHz. FHW observes a relatively narrow but expanding patch of backscatter flowing in the westward direction. At the same time CVE observes a narrow patch of bistatic scatter with low velocities. The CVE measurements during this interval are thought to be propagating in the bistatic IS mode. We have selected the period at 01:44 UT, marked by the vertical magenta line in all panels of Figure 9, to investigate this mode in more detail. Note that during the daytime hours both the direct mode and bistatic GS mode are also observed by CVE on this day.

Figure 10 shows measurements from all four SuperDARN radars during the 1-min scan period beginning at 01:44 UT on 1 October 2019 in which each radar samples 20 beam directions for 3 s each. The main backscatter feature during this time is the relatively narrow (<10° AACGM latitude) channel of westward directed flow seen by the three radars operating monostatically (CVW, FHW and FHE). The sense of the LOS flow alternates between toward and away across the three radars as the dominant sense of azimuthal direction of radar FOV alternates. The gray color seen in the FHW FOV indicates where the flow direction is perpendicular to the radar beam direction, and hence, V_{LOS} is close to zero. Analysis of the azimuthal dependence of V_{LOS} for this period indicates that the measurements are consistent with westward directed flow that is increasing in magnitude the further west the flow is measured, suggesting that the radars are observing a relatively low-velocity subauroral polarization stream (SAPS) (Foster & Burke, 2002; Kunduri et al., 2018).

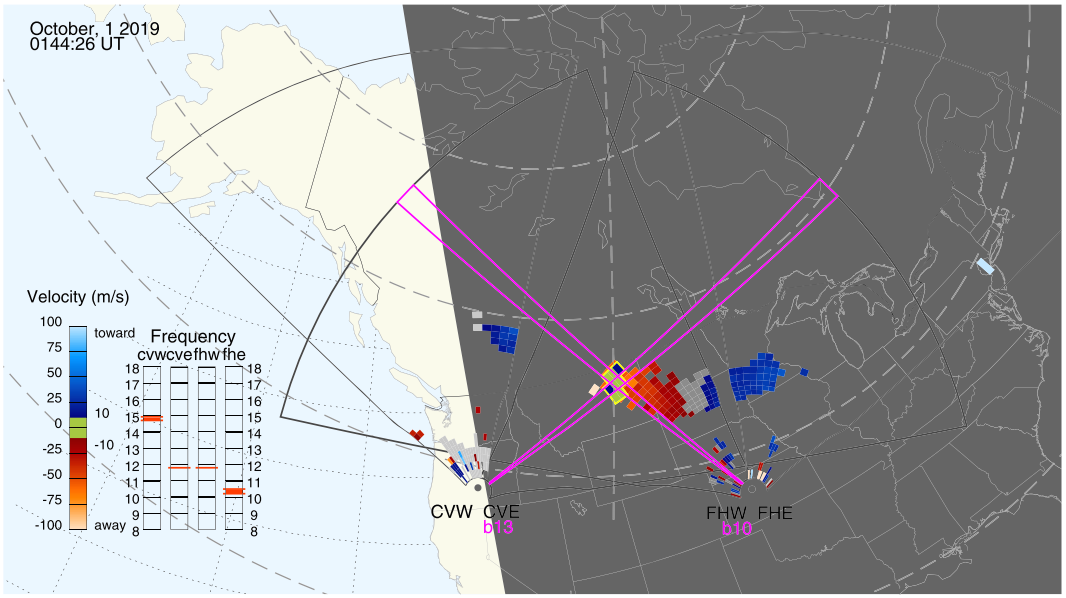

Figure 10. SuperDARN observations for a 1-min period from 01:44 UT on 1 October 2019 during a bistatic campaign. LOS Doppler velocity (V_{LOS}) shown in a similar manner to Figure 4 reveals a channel of subauroral westward flow in the FOVs of three monostatic radars. Coincident bistatic measurements from CVE, highlighted in yellow, show a region of scatter propagating in the bistatic IS mode where measurements from FHW coincide with the bisector of the radar sites (dashed line).

The signal observed by the bistatic receiver at CVE is highlighted in yellow in Figure 10. The extent of these measurements is limited, but as was the case with the bistatic GS mode, the measurements occur where the CVE beam overlaps the monostatic observations from FHW that reveal the relatively narrow SAPS channel. In this case the observations occur along the radar site bisector due to the symmetric beam sampling that was used during this period. These signals, which propagate in the bistatic IS mode, are transmitted from FHW and refract in the ionosphere before scattering from ionospheric density irregularities. The signal that returns to FHW is the standard ionospheric backscatter observed during monostatic operations, while the signal observed by CVE has been scattered by irregularities in the direction of the bistatic receiver. In addition, the bistatic geometry requires the presence of ionospheric irregularities with a larger scale size than those needed in the monostatic case (cf. Fejer & Kelley, 1980, p. 402). For the beam combinations with which the bistatic IS mode is observed during this period, the scattering irregularities are a factor of ~1.30–1.45 larger in scale length than those responsible for the observed monostatic ionospheric backscatter.

The basic concept of the bistatic GS mode and the bistatic IS mode is the same; signals are transmitted from the one radar, refract in the ionosphere, and are then scattered in the direction of the second, receive-only radar. The difference is in the scattering mechanism. For the bistatic GS mode signals are scattered from the ground or sea whereas irregularities in the ionosphere are the source of scattering for the bistatic IS mode. Unlike the bistatic GS example, no direct mode was observed during this time.

On this day, as seen in Figure 9, the magnitude and extent of the SAPS channel observed by the monostatic radars were quite variable and as a result the bistatic IS mode was only observed during a limited time. The Doppler V_{LOS} observed by the radars during this time was likewise variable. For the monostatic radars the largest values of V_{LOS}, up to ~70 m s^{-1}, were observed by the FHW radar during the period of 01:40–01:50 UT. If we assume the flow direction is perpendicular to the beam azimuth where zero-flow is observed by the FHW radar and scale V_{LOS} by beam azimuth, the observed velocities increase to ~200 m s^{-1}.

The bistatic IS mode observations by CVE occur in the region where the highest velocities were observed by FHW; however, the observed bistatic velocities were much smaller. For the same period, V_{LOS} ranged from 0–30 m s^{-1} at CVE, with a weighted-mean of ~15 m s^{-1}. While these velocities are relatively small, and in fact satisfy the ground scatter criteria, they can be explained by the bistatic viewing geometry. In the case

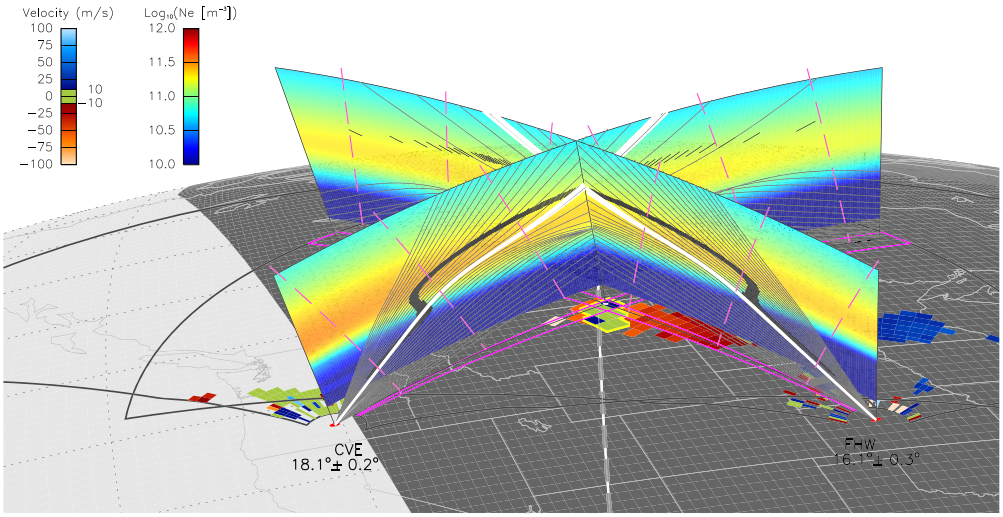

Figure 11. SuperDARN observations and ray tracing simulations at 01:44 UT on 1 October 2019. A subauroral flow channel is observed by the monostatic radars with V_{LOS} reaching 50 m s^{-1}. Bistatic measurements are observed along the bisector line where the CVE beams overlap observations from FHW. Ray tracing simulations along representative beam directions from CVE and FHW show raypaths (highlighted in white), which intersect at *F* region altitudes and the ray k-vectors are perpendicular to the *B* field (marked by black line-segments along rays). If ionospheric irregularities are present at the intersection location, signals are backscattered to the transmitting radar in addition to propagating in the bistatic IS mode to the receiving bistatic radar.

of bistatic measurements the Doppler component observed by the receiving radar is in the direction of the bisector of the transmitting and receiving beams (Atlas et al., 1968). For this example symmetric beam sampling is used and the direction is therefore along the site bisector line, which in this case is roughly perpendicular to the westward directed flow resulting in small velocities.

While the small velocities of the bistatic IS mode observations do help to define the direction of the flow in the region where monostatic and bistatic measurements are made, it also makes it somewhat challenging to determine on the basis of velocity magnitude alone whether measurements are propagating in the bistatic GS or the bistatic IS mode. For these reasons we have begun making bistatic observations using nonsymmetric beam sampling in order to measure a more significant component of the flow with the bistatic receiving radar. The larger velocities will make it easier to identify the bistatic propagation mode but will require further development to properly interpret measurements where the transmission and reception legs are no longer symmetric.

We perform a similar ray tracing simulation with the bistatic IS mode observations in order to confirm that this mode was viable during this period. Figure 11 shows the ray tracing results for the 1-min period beginning at 01:44 UT on 1 October 2019. As with the simulation of the bistatic GS mode, radar measurements during this time are shown on the map. The electron density obtained from the IRI-2016 model for this period is shown along the same beam directions displayed in Figure 7. Of particular note is the lower electron density for this period, as would be expected during the nighttime when solar ionization is absent and recombination reduces the ionospheric density.

One addition to Figure 11 is the short black line-segments, which indicate the location along individual raypaths where the wave k-vector is perpendicular to the local magnetic field (indicated by vertical pink lines). These locations show where conditions exist for the signal to be backscattered to the transmitting radar. In the case of monostatic operation these mark the locations where radar backscatter would be expected in the presence of suitable irregularities. In fact, FHW observed backscatter that is consistent with this geometry.

While a full three-dimensional analysis of the scatter region and resulting propagation along the reception path is required for bistatic operations, we again choose to demonstrate the viability of this mode by performing ray tracing from CVE to the potential scattering region and assuming that reciprocity holds. We highlight the rays in white that satisfy the conditions for signals propagating in the bistatic IS mode, that is, the rays

that are within 1° of perpendicularity to the local magnetic field in the region where the bistatic radar beams intersect. These are the rays for which the bistatic IS mode is a viable propagation path for bistatic observations during this time.

The simulations for the other beam combinations used during this period show that the elevation angles of the bistatic IS mode rays were in the range 15°–19°. Because bistatic IS mode observations were limited during this period we look at elevation angles measured by CVE over the 1-hr period 01:00–02:00 UT. Figure 8 (right panel) shows elevation angle occurrence histograms for CVE Beam 13 in orange and for comparison, CVW Beam 20 in blue. During this period lower counts are observed by both radars, largely due to the narrow features producing the measurements. Despite the lower count there is a well-defined peak in the CVW histogram at ~17.5°. The elevation angles observed by CVE are more variable but do show a peak at ~12.5°. While this value is somewhat lower than what is shown in the simulations, we reiterate that no modifications to the densities obtained from the IRI-2016 model were performed, as likely should be carried out to more nearly match the more geomagnetically disturbed conditions. We reserve such analyses for future studies and acknowledge that while differences exist between the simulation outputs and observations, the overall consistency confirms that the bistatic observations were supported by the ionosphere in the manner we have described.

4. Summary

SuperDARN radars operate primarily in a monostatic configuration in which HF signals transmitted from a radar propagate in the ionosphere and backscatter from ionospheric density irregularities at *E* region or *F* region altitudes, or from the Earth's surface, before returning to the same radar. These radars cover a large portion of the Earth's polar regions and measurements from the network are used in numerous studies of the thermosphere-ionosphere-magnetosphere system (Chisham et al., 2007).

We have developed the necessary hardware and software to operate, for the first time, SuperDARN HF radars in a bistatic manner whereby HF signals transmitted from one radar are received and analyzed by another radar that is separated by a distance >1,000 km. Initial testing with radars located in Oregon and Kansas confirms that sufficient timing accuracy is achieved for bistatic operation by using GPS synchronized clocks. Furthermore, the imposed frequency separation with the colocated second radar at these dual-radar sites prevents any unwanted signals due to coupling.

A series of 3-day bistatic campaigns were performed over a period from September 2019 to March 2020 in which the CVE radar in Oregon was operating bistatically with the FHW radar located in Kansas. During these campaigns signals transmitted by FHW were received and analyzed by the CVE radar. The nonbistatic radars, CVW and FHE, and the FHW radar, received and analyzed their own signals, providing contextual information about the ionosphere in the nearby region.

During the campaigns numerous bistatic observations were made and three distinct modes were identified:

1. Direct mode—HF signals are transmitted from FHW and received by CVE through radar side lobes in the vertical plane defined by the great-circle arc along the Earth's surface that joins the sites. Refraction from both *E* region and *F* region altitudes can occur independently or simultaneously, depending on the ionospheric densities along the propagation path between the bistatic radars. This mode is observed over a fixed range interval, often in all beam directions but with varying amplitude, and is more commonly seen during the daytime when ionospheric densities are largest.
2. Bistatic ground scatter mode—HF signals propagate from the transmitting radar (FHW) into the ionosphere and refract back toward the Earth where they are scattered from the surface. For monostatic radars the scattered signal propagates back to the transmitting radar along the same path. For the bistatic GS mode the scattered signal propagates along a similar path in the direction of the bistatic receiver, CVE in this case. Bistatic GS mode scatter is observed where the two radar beams overlap and ground backscatter is observed by the transmitting radar in its monostatic configuration. For the case where the beams are scanned symmetrically, the intersection point occurs along the radar site bisector.
3. Bistatic ionospheric scatter mode—HF signals propagate in a similar manner to the bistatic GS mode, however, scattering occurs from ionospheric density irregularities. Backscatter is received on the monostatic transmitter and the observed Doppler V_{LOS} is a component of the $E \times B$ drift velocity (assuming the

backscatter occurs at *F* region altitudes). Scatter received by the bistatic radar propagates in the bistatic IS mode and the observed Doppler V_{LOS} is in the direction that bisects the transmission and reception beams. As with the bistatic GS mode, bistatic IS mode observations occur where radar beams intersect and backscatter is observed by the transmitting radar.

In order to explain the various modes of propagation that were observed during bistatic operation, we performed ray tracing simulations for examples of each of the three modes. The simulations were performed using electron densities specified by the IRI-2016 model in the vertical planes appropriate to the various propagation modes. In all cases electron densities were unmodified from the values obtained by the IRI-2016 model and the agreement between the predicted and observed propagation paths of bistatic scatter observations varied but was generally reasonable.

The purpose of this work was to present the first bistatic measurements made by two SuperDARN HF radars. Analysis demonstrates that the propagation modes observed in cases where the paths along the respective transmission and reception legs are similar is well-understood. For observations that are made when the propagation paths are dissimilar, more detailed analyses are being developed to better understand the measurements. In addition, software and hardware development continues in order to improve synchronization between bistatic radar sites and the resulting bistatic measurements.

Data Availability Statement

The raw SuperDARN data are available from the British Antarctic Survey (BAS) SuperDARN data server (https://www.bas.ac.uk/project/superdarn). Software for the IRI-2016 model is available online (http://irimodel.org).

Acknowledgments

This research was funded by the Air Force Research Laboratory (AFRL) Space Environment Exploitation and Mitigation program under Cooperative Research Agreement FA9453-18-2-0032, and by a joint agreement between the National Science Foundation (NSF) and AFRL under NSF Grant AGS-1341918, and by the Air Force Office of Scientific Research under the Global Ionospheric Processes task. Additional funding for operations of U.S. SuperDARN radars is provided by NSF Grants AGS-1341925 and AGS-1934997 (for Dartmouth College); AGS-1341918 and AGS-1935110 (for Virginia Tech).

References

André, D., Sofko, G. J., Baker, K., & MacDougall, J. (1998). SuperDARN interferometry: Meteor echoes and electron densities from groundscatter. *Journal of Geophysical Research*, *103*(A4), 7003–7015. https://doi.org/10.1029/97JA02923

Atlas, D., Naito, K., & Carbone, R. E. (1968). Bistatic microwave probing of a refractively perturbed clear atmosphere. *Journal of the Atmospheric Sciences*, *25*, 257. https://doi.org/10.1175/1520-0469(1968)025

Baker, K. B., Greenwald, R. A., Ruohoniemi, J. M., Dudeney, J. R., Pinnock, M., Mattin, N., & Leonard, J. M. (1989). PACE polar Anglo-American conjugate experiment. *Eos, Transactions American Geophysical Union*, *70*, 785.

Baker, J. B. H., Greenwald, R. A., Ruohoniemi, J. M., Oksavik, K., Gjerloev, J. W., Paxton, L. J., & Hairston, M. R. (2007). Observations of ionospheric convection from the wallops SuperDARN radar at middle latitudes. *Journal of Geophysical Research*, *112*, A01303. https://doi.org/10.1029/2006JA011982

Berngardt, O. I., Kutelev, K. A., Kurkin, V. I., Grkovich, K. V., Kashcheyev, S. B., Galushko, V. G., et al. (2015). Bistatic sounding of high-latitude ionospheric irregularities using a Decameter EKB radar and an UTR-2 radio telescope: First results. *Radiophysics and Quantum Electronics*, *58*, 390–408. https://doi.org/10.1007/s11141-015-9614-1

Bilitza, D., Altadill, D., Truhlik, V., Shubin, V., Galkin, I., Reinisch, B., & Huang, X. (2017). International Reference Ionosphere: 2016 From ionospheric climate to real-time weather predictions. *Space Weather*, *15*, 418–429. https://doi.org/10.1002/2016SW001593

Blanchard, G. T., Sundeen, S., & Baker, K. B. (2009). Probibilistic identification of high-frequency radar backscatter from the ground and ionosphere based on spectral characteristics. *Radio Science*, *44*, RS5012. https://doi.org/10.1029/2009RS004141

Chisham, G., Lester, M., Milan, S. E., Freeman, M. P., Bristow, W. A., Grocott, A., et al. (2007). A decade of the Super Dual Auroral Radar Network (SuperDARN): Scientific achievements, new techniques and future directions. *Surveys in Geophysics*, *28*, 33–109. https://doi.org/10.1007/s10712-007-9017-8

Chisham, G., & Pinnock, M. (2002). Assessing the contamination of SuperDARN global convection maps by non-F-region backscatter. *Annales Geophysicae*, *20*, 13. https://doi.org/10.5194/angeo-20-13-2002

de Larquier, S., Ponomarenko, P., Ribeiro, A. J., Ruohoniemi, J. M., Baker, J. B. H., Sterne, K. T., & Lester, M. (2013). On the spatial distribution of decameter-scale subauroral ionospheric irregularities observed by SuperDARN radars. *Journal of Geophysical Research*, *118*, 5244–5254. https://doi.org/10.1002/jgra.50475

Fejer, B. G., & Kelley, M. C. (1980). Ionospheric irregularities. *Reviews of Geophysics*, *18*, 401–454. https://doi.org/10.1029/RG018i002p00401

Foster, J. C., & Burke, W. J. (2002). SAPS: a new categorization for sub-auroral electric fields. *Eos, Transactions American Geophysical Union*, *83*(36), 393–394.

Greenwald, R. A., Baker, K. B., Dudeney, J. R., Pinnock, M., Jones, T. B., Thomas, E. C., et al. (1995). DARN/SuperDARN: A global view of the dynamics of high-latitude convection. *Space Science Reviews*, *71*, 761. https://doi.org/10.1029/95JA01215

Greenwald, R. A., Baker, K. B., Hutchins, R. A., & Hanuise, C. (1985). An HF phased-array radar for studying small-scale structure in the high-latitude ionosphere. *Radio Science*, *20*, 63. https://doi.org/10.1029/RS020i001p00063

Hughes, J. M., Bristow, W. A., Greenwald, R. A., & Barnes, R. J. (2002). Determining characteristics of HF communications links using SuperDARN. *Annales Geophysicae*, *20*, 1023–1030. https://doi.org/10.5194/angeo-20-1023-2002

Kunduri, B. S. R., Baker, J. B. H., Ruohoniemi, J. M., Nishitani, N., Oksavik, K., Erickson, P. J., et al. (2018). A new empirical model of the sub-auroral polarization stream. *Journal of Geophysical Research*, *123*, 7342–7357. https://doi.org/10.1029/2018JA025690

Nishitani, N., Ruohoniemi, J. M., Lester, M., Baker, J. B. H., Koustov, A. V., Shepherd, S. G., et al. (2019). Review of the accomplishments of mid-latitude Super Dual Auroral Radar Network (SuperDARN) HF radars. *Progress in Earth and Planetary Science*, *6*(27), 1–57. https://doi.org/10.1186/s40645-019-0270-5

Perry, G. W., James, H. G., Gillies, R. G., Howarth, A., Hussey, G. C., McWilliams, K. A., et al. (2017). First results of HF radio science with e-POP RRI and SuperDARN. *Radio Science*, *52*, 78–93. https://doi.org/10.1002/2016RS006142

Ponomarenko, P., Nishitani, N., Oinats, A. V., Tsuya, T., & St.-Maurice, J.-P. (2015). Application of ground scatter returns for calibration of HF interferometry data. *Earth Planets Space*, *67*, 138. https://doi.org/10.1186/s40623-015-0310-3

Ribeiro, A. J., Ruohoniemi, J. M., Ponomarenko, P. V., Clausen, L. B. N., Baker, J. B. H., Greenwald, R. A., et al. (2013). A comparison of SuperDARN ACF fitting methods. *Radio Science*, *48*, 274–282. https://doi.org/10.1002/rds.20031

Ruohoniemi, J. M., & Baker, K. B. (1998). Large-scale imaging of high-latitude convection with Super Dual Auroral Radar Network HF radar observations. *Journal of Geophysical Research*, *103*(20), 797. https://doi.org/10.1029/98JA01288

Ruohoniemi, J. M., Barnes, R. J., Greenwald, R. A., & Shepherd, S. G. (2001). The response of the high-latitude ionosphere to the coronal mass ejection event of April 6, 2000: A practical demonstration of space weather nowcasting with the Super Dual Auroral Radar Network HF radars. *Journal of Geophysical Research*, *106*(30), 85. https://doi.org/10.1029/2000JA000217

Ruohoniemi, J. M., & Greenwald, R. A. (1997). Rates of scattering occurrence in routine HF radar observations during solar cycle maximum. *Radio Science*, *32*, 1051–1070. https://doi.org/10.1029/97RS00116

Samson, J. C., Greenwald, R. A., Ruohoniemi, J. M., Frey, A., & Baker, K. B. (1990). Goose Bay radar observations of Earth-reflected, atmospheric gravity waves in the high-latitude ionosphere nightside magnetosphere. *Journal of Geophysical Research*, *95*, 7693–7709. https://doi.org/10.1029/JA095iA06p07693

Shepherd, S. G. (2014). Altitude-adusted corrected geomagnetic coordinates: Definition and functional approximations. *Journal of Geophysical Research*, *119*, 7501–7521. https://doi.org/10.1002/2014JA020264

Shepherd, S. G. (2017). Elevation angle determination for SuperDARN HF radar layouts. *Radio Science*, *52*, 938–950. https://doi.org/10.1002/2017RS006348

Sterne, K. T., Greenwald, R. A., Baker, J. B. H., & Ruohoniemi, J. M. (2011). Modeling of a twin terminated folded dipole antenna for the Super Dual Auroral Radar Network (SuperDARN), *2011 IEEE RADAR CONFERENCE (RADAR), IEEE National Radar Conference Proceedings* pp. 934–938). NEW YORK, NY 10017 USA: IEEE, 345 E 47TH ST. https://doi.org/10.5594/SMPTE.RP2079.2013

Thébault, E., Finlay, C. C., Beggan, C. D., et al. (2015). And International Geomagnetic Reference Field: The 12th generation. *Earth Planets Space*, *67*, 79. https://doi.org/10.1186/s40623-015-0228-9

Thomas, E. G., Sterne, K. T., Shepherd, S. G., Kotyk, K., Schmidt, M., Ponomarenko, P. V., et al. (2019). SuperDARN Radar Software Toolkit (RST) 4.3. https://doi.org/10.5281/zenodo.3401622

Wright, D. M., & Yeoman, T. K. (1999). High resolution bistatic HF radar observations of ULF waves in artificially generated backscatter. *Geophysical Research Letters*, *26*, 2825–2828. https://doi.org/10.1029/1999GL900606

Yeoman, T. K., Baddeley, L. J., Dhillon, R. S., Robinson, T. R., & Wright, D. M. (2008). Bistatic observations of large and small scale ULF waves in SPEAR-induced HF coherent backscatter. *Annales Geophysicae*, *26*(8), 2253–2263. https://doi.org/10.5194/angeo-26-843-2008